Topology Optimization of Segmented Thermoelectric Generators

Lundgaard, Christian; Sigmund, Ole; Bjørk, Rasmus

Published in:
Journal of Electronic Materials

Link to article, DOI:
10.1007/s11664-018-6606-x

Publication date:
2018

Document Version
Peer reviewed version

Noname manuscript No.
(will be inserted by the editor)

Topology optimization of segmented thermoelectric generators

Christian Lundgaard[a], **Ole Sigmund**[b], **Rasmus Bjørk**[c]

the date of receipt and acceptance should be inserted later

Abstract The thermoelectric (TE) power output, f_P, and conversion efficiency, f_η, for segmented thermoelectric generators (TEGs) are optimized by spatially distributing two TE materials (BiSbTe and Skutterudite) using a numerical gradient-based topology optimization approach. The material properties are temperature dependent and the segmented TEGs are designed for various heat transfer rates at the hot and cold reservoirs. The topology optimized design solutions are characterized by spike-shaped design features which enable the designs to operate in an intermediate state between the material phases. Important design parameters, such as the device dimensions, objective functions and heat transfer rates, are identified, investigated and discussed. Comparing the topology optimization approach with the classical segmentation approach, the performance improvements of f_P and f_η design problems depend on the heat transfer rates at the hot and the cold reservoir, the objective function and the device dimensions. The largest performance improvements for the problems investigated are ≈6%.

Keywords: Topology optimization, thermoelectric energy conversion, electric power output, conversion efficiency

[a] Department of Mechanical Engineering
Techinical University of Denmark, Nils Koppels Allé Building 404, DK-2800 Kgs. Lyngby, Denmark
E-mail: chrlund@mek.dtu.dk
[b] Department of Mechanical Engineering
Techinical University of Denmark, Nils Koppels Allé Building 404, DK-2800 Kgs. Lyngby, Denmark
E-mail: sigmund@mek.dtu.dk
[c] Department of Energy Conversion and Storage
Technical University of Denmark, Frederiksborgvej 399, DK-4000 Roskilde, Denmark
E-mail: rabj@dtu.dk

1 Introduction

Thermoelectric generators (TEGs) are used to transform thermal energy into electric energy by utilizing the Seebeck effect [1]. TEGs are applicable in converting thermal energy from numerous sources such as exhaust gasses of combustion engines, heat exchangers and solar devices. The increasing demand on green and sustainable energy resources, and the capability of TEGs to convert waste heat into electric energy, have positioned TEGs as a possible focal entrant in the global green energy source changeover. However, the unrolling of large-scale industrial applications of TEGs are limited by the performance of the technology [2], thus these performance limitations have attracted a considerable amount of scientific attention in recent decades.

High performing TEGs are characterized by maintaining a high ratio between the electric energy output and the thermal energy input. At least three measures are important in relation to the performance of TEGs: The thermoelectric figure-of-merit, ZT, the electric power output, f_P, and the conversion efficiency, f_η. In this study we will discuss the latter two.

It has previously been shown that the performance of TEGs can be significantly increased by *segmentation* [3, 4]. Segmentation approaches take basis in finding materials which are *compatible*. Compatible materials operate optimally under the same external electrical resistance and are therefore suited for operation thermally and electrically in series. The segmentation approach is characterized by design solutions where the material phases are separated by one dimensional line interfaces. We will in this paper refer to this type of approaches as *classical segmentation*.

The density-based topology optimization approach utilized in this study is related to the classical segmen-

tation approach, as the design problems take basis in distributing two different thermoelectric active materials in order to optimize for some performance measure. The main difference between the two approaches is, that the topology optimization approach takes two dimensional features in the design solutions into consideration, where the classical segmentation approach is limited to one dimensional features.

The topology optimization approach [5, 6] is based on a finite element formulation of the generalized Ohm's and Fourier's law [7] and the topology optimization methodology described in Lundgaard and Sigmund [8]. Compared to analytic approaches, the finite element formulation makes it possible to take more advanced physical modelling concepts into consideration such as temperature dependent material parameters, complex geometries and advanced boundary conditions. The objective of the design problems is to optimize f_P and f_η, which both are measures that reflect the practical applications of TEGs. In comparison to optimization approaches which aim to maximize the thermoelectric figure-of-merit of the material phases over the device [9], this optimization strategy may be better suited for real applications of TEGs. Thermoelectric materials are governed by three material parameters: the Seebeck coefficient, α, the electric conductivity, σ, and the thermal conductivity, κ. For real materials, the material parameters are temperature dependent and some materials degenerate for temperatures above specific magnitudes. These relationships are all taken into consideration in this study.

TEGs utilize the temperature difference between a hot and a cold reservoir to convert thermal energy into electric energy. The performance of TEGs is among other parameters governed by the size of the reservoirs and the magnitude of the thermal heat transfer at the boundaries [8, 10–12]. Studies of TEGs with limited heat transfer have been investigated for various problems such as micro-heat exchangers [13–15], air-to-air heat exchangers [16–19], as well as fluid-based heat exchangers [20–25].

The heat transfer rate between the TEG and the thermal reservoirs is characterized by the governing thermal energy convection mechanisms, and depends on the fluid type and the flow type in the thermal reservoirs. The heat transfer rate is quantized by heat transfer coefficients, h^H (H refers to *hot*) and h^C (C refers to *cold*) for the hot and the cold reservoirs, respectively. The heat transfer coefficients are related to the thermal resistance of the contact between the TEG and the source as $R_T = \frac{1}{hA}$ where A is the area of the contact.

With basis in real temperature dependent materials, realistic boundary condition and model parameters, we demonstrate that a density-based topology optimization approach can be utilized to optimize f_P and f_η for TEGs. The design solutions are driven by spatially determining the layout of two different thermoelectric materials in a two dimensional domain. We demonstrate that the topology optimized design solutions are never worse and may outperform the classical segmentation approach design solution for some choices of model parameters. Furthermore, we state and discuss several important parameters which influence the design solutions and should be taken into consideration when designing TEGs.

2 The optimization problem

In this section we briefly present the concept of the density-based topology optimization framework which is utilized to optimize the TEGs. We introduce several variables throughout the paper and for readability purposes, we have summarized the most important ones in Tab. 1.

2.1 Physical model

The optimization problem takes basis in the sketch in Fig. 1. A thermoelectric module, Ω_D, is separated by

Table 1: List of important variables

Variable	Description
Γ^H	Boundary at the *hot* reservoir
Γ^C	Boundary at the *cold* reservoir
Γ^{HC}	Abbreviation of Γ^H and Γ^C combined
T^H	Temperature in the *hot* reservoir
T^C	Temperature in the *cold* reservoir
T^{HC}	Abbreviation of T^H and T^C combined
h^H	Convection coefficient at Γ^H
h^C	Convection coefficient at Γ^C
h^{HC}	Abbreviation of h^H and h^C combined
$\mathbf{T}$	The temperature field [K]
$\mathbf{V}$	The electric potential field [V]
$\mathbf{Q}_x, \mathbf{Q}_y$	The thermal heat flux field in x and y, respectively
$\mathbf{J}_x, \mathbf{J}_y$	The electric current density field in x and y, respectively
f_P	Electric power output
f_η	Conversion efficiency
Ω_D	Design domain
L_x	Length of Ω_D in x
L_y	Length of Ω_D in y

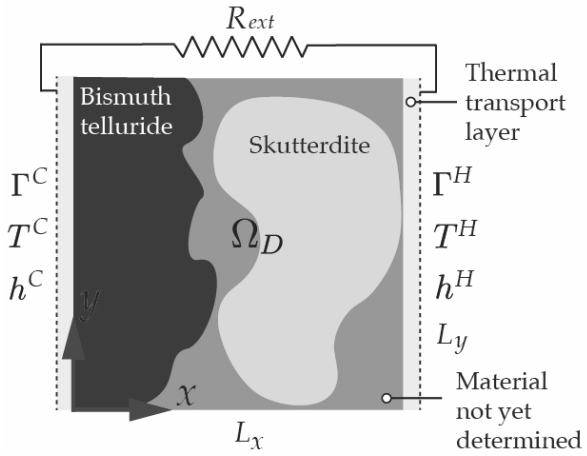

Fig. 1: Schematic of the design problem. The distribution of skutterudite and BiSbTe in Ω_D is determined with density-based topology optimization in order to optimize for f_P or f_η.

a thermally hot and a cold reservoir with boundaries Γ^H and Γ^C, respectively. The heat transfer between the thermoelectric module and the hot and cold reservoirs is modelled by a limited heat transfer with heat transfer coefficients, h^H and h^C, and temperatures, T^H and T^C. If the convection coefficients or the temperatures on Γ^H and Γ^C are equal, the variables are simply denoted h^{HC} and T^{HC}, respectively.

The basic partial differential equations of thermoelectricity are constrained by Fourier's and Ohm's generalized law. With reference to Fig. 1, the continuity of thermal energy and electric charge are in Ω_D given by [1]:

$$\nabla \cdot \mathbf{Q} = \dot{q} \quad \text{in} \quad \Omega_D \tag{1}$$

$$\nabla \cdot \mathbf{J} = 0 \quad \text{in} \quad \Omega_D \tag{2}$$

where ∇ denotes the spatial derivative with respect to Cartesian directions x and y; $\mathbf{Q} = \{Q_x, Q_y\}$ is the heat flow density in x and y [W/m^2]; $\dot{q} = \mathbf{J} \cdot \mathbf{E}$ is the Joule heating term [W/m^3]; $\mathbf{E} = -\nabla V$ is the electric field [V/m]; V is the electric potential and $\mathbf{J} = \{J_x, J_y\}$ is the electric current density in x and y [A/m^2]. In thermoelectric analysis, the thermal and electric energies are coupled by the constitutive equations:

$$\mathbf{Q} = T\alpha \cdot \mathbf{J} - \kappa \cdot \nabla T \tag{3}$$

$$\mathbf{J} = \sigma \cdot (\mathbf{E} - \alpha \cdot \nabla T) \tag{4}$$

where T is the temperature [K], α is the Seebeck coefficient, κ is the electric conductivity and σ is the electric conductivity.

Table 2: Heat transfer due to convection coefficients for various flow types and flow conditions

Flow type	Flow condition	h [W/m^{2}K]
Forced convection	Air over a surface	100
	Air over a cylinder	200
	Water in a pipe	3000
Free convection	Water and liquids	50-3000
	Water	100-1200
	Air	10-100
	Various gasses	5-37

2.1.1 Resistive load

The electric current in the external resistive load (see Fig. 1) is given by:

$$\mathbf{n} \cdot \mathbf{J} = R_{ext}(V - V^C) \tag{5}$$

where $\mathbf{n}$ is a vector normal to the surface, R_{ext} is the resistance of the resistive load [m/S] and V^C is the reference electric potential [V] on Γ^C.

2.1.2 Newton's law of cooling

With reference to the simple rectangular design and the relatively small length scales of TEG modules in Fig. 1, we assume that an adequate modelling approach for the heat transfer between the hot and the cold reservoirs and the TEG module is *Newton's law of cooling*. Newton's law of cooling assumes that the thermal heat transfer between thermal hot and cold reservoirs and the module is proportional to the difference in temperatures between these:

$$\mathbf{n} \cdot \mathbf{Q} = h^{HC}(T - T^{HC}) \tag{6}$$

where h^{HC} denotes the convection coefficient [W/m^{2}K] on Γ^H (h^H) and Γ^C (h^C), respectively, and T^{HC} denotes the temperatures of the thermal reservoirs [K] in Γ^H (T^H) and Γ^C (T^C), respectively.

By utilizing Eq. (6), it is assumed that the thermal heat transfer between the thermal hot and cold reservoirs and the module is proportional to the difference in temperatures between the body and its surroundings and that the temperatures of the reservoirs are constant along Γ^H and Γ^C. We believe that these assumptions are adequate for this specific problem, however, in detailed computations the thermal heat transfer should be modelled taking local convection, diffusion and radiation into account. h^{HC} in Eq. 6 can be experimentally determined and some values for different flow types and flow conditions are listed in Table 2.

2.1.3 Material parameters

The TEGs are optimized with respect to f_P and f_η by spatially determining the distribution of BiSbTe [26] and $NdFe_{3.5}Co_{0.5}Sb_{12}$ (skutterudite) [27] in Ω_D (see Fig. 1). BiSbTe and skutterudite are p-type semi-conducting and temperature dependent materials. The relationships between α, σ, κ, $Z = \alpha^2\sigma/\kappa$ and the temperature for both materials are plotted in Fig. 2. BiSbTe has a maximum operation temperature of 540 K, because it is chemically unstable for higher temperatures. To ensure that the BiSbTe material phases is not subjected to a too large operating temperature, we impose a temperature constraint on the BiSbTe material phase. Details on the implementation of the temperature constraint can be found in Sec. 6. BiSbTe and skutterudite are compatible materials [28], and have previously been shown to have an increased efficiency in a classically segmented configuration compared to the constitutive materials [4, 29]. Compatible materials operate optimally under the same external resistance and are therefore suited for classical segmentation. According to [28], thermoelectric materials are compatible if their so-called *compatibility factor* does not exceed a ratio larger than 3. BiSbTe and Skutterudite in Fig. 2 have a compatibility factor of 2.1 for the plotted temperature range.

2.1.4 Finite element model

To set up the topology optimization framework, we introduce a spatial design field $0 \leq \rho \leq 1$, such that Eqs. (1)-(4) become functions of the design field, i.e. $\alpha(T) = \alpha(T, \rho)$, $\sigma(T) = \sigma(T, \rho)$ and $\kappa(T) = \kappa(T, \rho)$.

By doing so, it is possible to obtain the discretized finite element equations suited for topology optimization by multiplying the strong forms of Eqs. (1)-(4) with a suitable test function; integrating over the domain; performing integration by parts of higher dimensions on relevant terms [7, 30, 31]; and introducing the design field dependent interpolation functions. After introduction of the design variable field, it is now possible to control whether an element represents the skutterudite or the BiSbTe material phase. The material phase is determined by computing the gradients of the objective function with an analytic adjoint sensitivity analysis. This outlines the fundamental concept of the topology optimization framework. Interested readers are referred to the detailed description of the implementation and concept of the density-based topology optimization framework in [8].

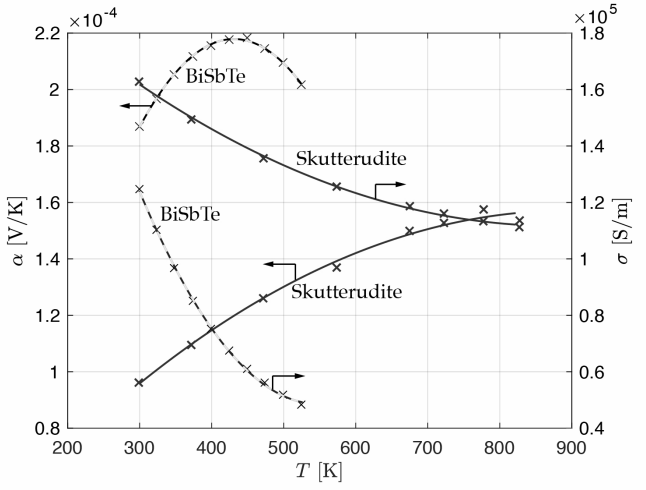

(a)

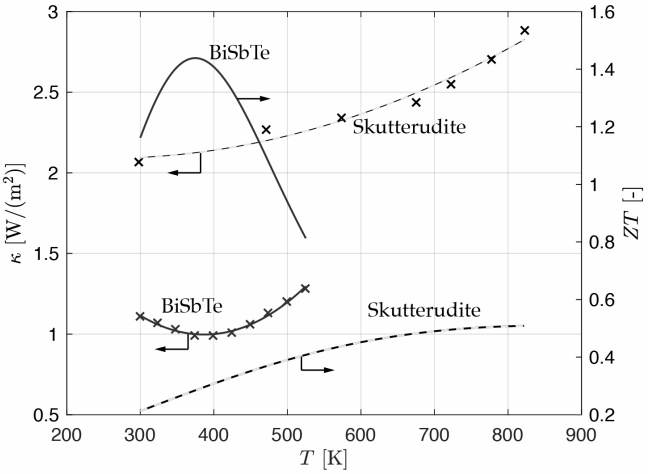

(b)

Fig. 2: The Seebeck coefficient and electric conductivity (a) and the thermal conductivity and figure-of-merit (b) as function of the temperature, T. The markers are experimental values and the continuous lines are the corresponding fitted interpolation functions.

2.1.5 The optimization problem

The optimization problem sketched in Fig. 1 has dimensions $L_x = 5$ [mm] and $L_y = 5$ [mm], and we aim to optimize f_P and f_η. To optimize f_P and f_η we need to compute the electric power output of the thermoelectric module:

$$f_P = \frac{1}{L_y} \int_{\Gamma^H} V \, \mathrm{d}S \int_{\Gamma^H} J_x \, \mathrm{d}S \tag{7}$$

This is simply an integral expression for the electric potential and the electric current density at the hot reservoir-electrode of the TEG. In one dimensional analysis, the expression is often written as: $P = JV$, where

P is the electric power, J is the electric current and V is the electric potential. The conversion efficiency is given by:

$$f_\eta = \frac{f_P}{f_Q} \tag{8}$$

where the heat flux, f_Q, is given by the two dimensional integral expression:

$$f_Q = \frac{1}{L_x} \int_{\Gamma^H} Q_x \, \mathrm{d}S \tag{9}$$

To ensure that the BiSbTe material phase is not subject to temperatures above $T_{max} = 540$ K, we impose the following constraint to the optimization problem:

$$f_C \leq \max(\mathbf{T}) - T_{max} \leq 0 \quad \forall \mathbf{T} \in \Omega_{\mathrm{BiSbTe}} \tag{10}$$

where f_C is the objective for the temperature constraint, Ω_{BiSbTe} is the BiSbTe material phase domains in the design solutions. A detailed description of the implementation of the temperature constraint in Eq. 10 is given in Sec. 6.

The gradients of the objective functions (sensitivities) in Eqs. (7)-(8) and the temperature constraint in Eq. (10), are found with the discrete adjoint method [6, 32]. The physical design variable field used in the finite element analysis is obtained by a Heaviside projection filter and a density filter operation [33, 34]. The design problems are limited to two dimensions, however, an extrusion of the design solutions in the third spatial direction may serve as a three dimensional interpretation of the design solutions.

3 Results

The optimized spatial distributions of the BiSbTe and skutterudite material phases of the thermoelectric module in Fig. 1 are determined for $h^{HC} \in [100; 2000]$ [W/K·m^2] in the design solutions presented in this section. These convection coefficients correspond to a large range of different flow types and flow conditions in Tab. 2, and turn out to provide topologically interesting and different design solutions.

3.1 Electric power output

The design solutions for the f_P-problem optimized for various h^{HC} have been plotted in Fig. 3. The plots suggest that the optimized topologies of the design solutions are dependent on h^{HC}: As h^{HC} is increased, the extent of the "spike"-shaped design features are decreased. For higher magnitudes of h^{HC} the temperature constraint is active, which pushes the BiSbTe material phase towards Γ^C in order to match the temperature requirements of the BiSbTE material phases. The spike-shaped design features are gradually rounded when h^{HC} is increased and the design solutions are approaching the one-dimensional design solutions which is seen in classic segmentation when $h^{HC} \to \infty$.

A discussion of the state fields (e.g. the temperature and electric potential) of the design solutions is given in Sec. 3.3.

The design solutions in Fig. 3 are two dimensional and the parasitic losses between the material phases are neglected. With an offset in an analytic optimization approach, [35] manufactured and experimentally tested design solutions which consisted of two materials with a considerable amount of transitions between material phases. Despite the neglection of the parasitic losses and the large area between the different materials, [35] found excellent agreements between the analytic predictions and the experimentally tested designs.

The complexity of the design solution presented in this study may be comparable to the complexity of the design solutions manufactured by Sakai and coworkers, for which reason we therefore assess that the design solutions are manufacturable with methodologies available today. However, if this is not the case we refer to the rapid advances in additive manufacturing and material science, and hereby predict that the design solutions such as the ones in Fig. 3 are realizable in the near future. Until that time, the design solutions presented in this study can serve as a theoretical benchmark for what is achievable by allowing two dimensional features in segmented thermoelectric legs. Even though it is general practice in many mathematical optimization approaches of thermoelectric energy conversion problems to neglect parasitic losses, see e.g. the work in [3, 36, 37], we emphasize the importance of taking parasitic losses into consideration in detailed computations.

Figure-3a-

3.2 Conversion efficiency

The f_η-design solutions for various h^{HC} have been plotted in Fig. 4. The same trends in design solutions are observed as for the f_P-design solutions in Sec. 3.1, however, the BiSbTe material phases are generally pushed toward Γ^H for the f_η design compared to the f_P design. This design feature may be due to the low κ of the BiSbTe material phase which is cost effective for f_η problems.

The design solutions in Fig. 3-4 are all solved for the temperature constraint stated in Eq. (10). For small

(a) (b) (c) (d) (e)

Fig. 3: f_P-design solutions for convection coefficients, h^{HC} [W/m^2 K], equal to $h^{HC} = 141$ (a), $h = 594$ (b), $h = 821$ (c), $h = 1047$ (d) and $h = 10^{10}$ (e). The blue and yellow material phases represent BiSbTe and skutterudite, respectively.

h^{HC} the temperature constraint is inactive because $\Delta T \to 0$ as $h^{HC} \to 0$ and hence $T < T_{max}$ at Γ^{HC}. The temperature constraint becomes active when the magnitude of h^{HC} is large enough to push the temperature at Γ^H above T_{max}. In such problems, the BiSbTE material phase is pushed toward Γ^C to fulfill the constraint. The constraint of the design problem ensures that the optimized TEG do not degenerate during operation. For more information and comparisons between design solutions, please consult Sec. 6.

3.3 State fields of a specific design

The temperature, the electric potential, the heat flux and current density for the f_P-design solution in Fig. 3c have been plotted in Fig. 5. The temperature field and the electric potential field are almost smoothly distributed with only small gradients in the y-direction despite the two dimensional features of the design solutions. As both Ohm's and Fourier's generalized laws, see Eq. (1)-(4) are diffusion equations, the small y-directional gradients in the state fields may be explained by the differences in the material parameters between the material phases and the length scales of the design solutions. These parameters are simply not large enough to generate a considerable difference in the state fields in the two material phases. However, by increasing the length-scale of the design problem and the difference in the material parameters, the y-directional gradients of temperature and electric potential fields will also increase.

The temperatures at Γ^H and Γ^C are not exactly T^H and T^C due to the finite h^{HC}. As h^{HC} is increased, the temperatures at boundaries Γ^H and Γ^C will approach T^H and T^C. The almost straight streamlines of the electric current density and the heat flux on Figs. 5c-5d suggest that only minor two dimensional effects are affecting the design solutions. However, the gradients in $\mathbf{Q}$ and $\mathbf{J}$ between the spike-shaped designs features are large, which indicate that the design features indeed affect the performance of the design.

The framework can straightforwardly be extended such that thermal heat transfer rates on the horizontal boundaries of the design solutions are taken into consideration. Taking such effect into consideration would change the design solutions considerably, however thermoelectric modules are almost always thermally insulated or periodically assembled for which reason the thermal heat transfer rates on Γ^{HC} are many magnitudes larger than the thermal heat transfer rates on the vertical boundaries. With basis in this argument, we hence argue that the isolation assumption is physically realistic, which is a shame from the topology optimization perspective, as a considerable amount of thermal heat transfer on vertical boundaries may cause much more topological interesting and complex design solutions and increase the difference in performance between the topology optimized and segmented design solutions.

The appearance of the spike-shaped design features may be explained by the following two reasons: (1) They increase the heat flux and electric conductivity in the skutterudite material regions. (2) They enable the design to operate in an intermediate state between the two different material phases. In optimization approaches with functionally graded materials, the material parameters are determined as function of the spatial coordinates of the design domain in order to optimize for some performance measure (see e.g. the work by Seifert et al. [38], Gerstenmaier and Wachutka [39]). The design problems presented in this work are related to functionally graded materials design problems, though the topology optimized design solutions consist of two distinct material phases, where the design solutions of functionally graded material design approaches conceptually consist of infinitely many.

(a) (b) (c) (d) (e)

Fig. 4: f_η-design solutions for convection coefficients, h^{HC} [W/m^2 K], equal to $h^{HC} = 141$ (a), $h^{HC} = 594$ (b), $h^{HC} = 821$ (c), $h^{HC} = 1047$ (d) and $h^{HC} = 10^{10}$ (e). The blue and yellow material phases represent BiSbTe and skutterudite, respectively.

3.4 Performance of the designs

The performance of the design solutions in Sec. 3.1 and 3.2 are quantified in Fig. 6, where the normalized performances, $\bar{f}_P$ and $\bar{f}_\eta$, are plotted as function of h^{HC} for the designs in Figs. 3-4. To clarify the differences between design performances, we have normalized the objectives with respect to the performance of a TEG consisting of a stand-alone skutterudite material phase. The h^{HC} values next to the lines indicate the h^{HC} at which the design was optimized. To present a fair comparison between the topology optimized design solutions and the classical segmentation approach, we computed the optimal segmented design solutions for the same h^{HC} as the topology optimized designs. The design performances of the classical segmentation approach are determined by finding the optimal ratio between skutterudite and BiSbTe while fulfilling the temperature constraints for each magnitude of h^{HC}. The performance of the classical segmented design solutions is identified by the "segmented" legend in Fig. 6. The performances of the design solutions are computed by the following approach: The design solutions in Fig. 6a are evaluated for a sequence of h^{HC} and each line in Fig. 6 refers to the design performances with respect to the performance measure indicated on the plots. For guidance we provide an example to read the graph: The red curve in Fig. 6a is the f_P-optimized design solution for $h^{HC} = 141$ (see Fig. 3a) evaluated for $h^{HC} = [100; 2000]$. With reference to Fig. 6, we notice that the design solutions perform equivalently or outperform design solutions optimized for other convection coefficients, the standalone skutterudite and the classical segmented design solutions. The best relative improvement of the topology optimized and classical segmented design solutions are obtained for $h^{HC} \to 0$.

Crosschecks are important to determine how much significance we may attribute to the features of the optimized designs in Fig. 3-4. The relationship between the performance and the design solutions in Fig. 6, demonstrates that the spike shaped design features indeed provide design improvements compared to the classical segmentation approach.

By comparing the performance of the topology optimized and the classical segmented design solutions (black curves with label "Segmented" in Fig. 6), we notice that the difference between the optimization approaches is decreased as $h^{HC} \to \infty$.

The maximum design improvements for the parameters investigated in this study are $\approx 5\%$ and $\approx 6\%$ for the f_P and f_η designs optimized for $h^{HC} = 141$, respectively. The difference between the two optimization approaches is decreasing as $h^{HC} \to \infty$. As h^{HC} reaches a specific magnitude, the two optimization approaches provide the same design solutions and hereby also the same performances. The topology optimization approach is therefore only advantageous for low h^{HC} problems for this set of material parameters and model parameters.

3.5 The relationship between design performance and leg length

The finite convection coefficients on Γ^H and Γ^C entail that the thermal heat transfer between the hot and the cold reservoirs is limited by the heat transfer rate. In finite element simulations or analytic studies where the temperature boundary conditions are fixed or where the heat inputs are imposed as a heat flux, the size of the thermal hot and cold reservoirs and the heat transfer rate at Γ^H and Γ^C are assumed infinitely large. Optimization problems solved for fixed temperature boundary conditions may therefore provide non-physical and meaningless design solutions. To investigate the importance of device thickness, L_x, in the design problems, we have plotted the f_P and f_η-design solutions for $L_x = \{10, 20, 30, 40, 50\}$ [mm] in Fig. 7-8. With reference to the figures, we notice that the design

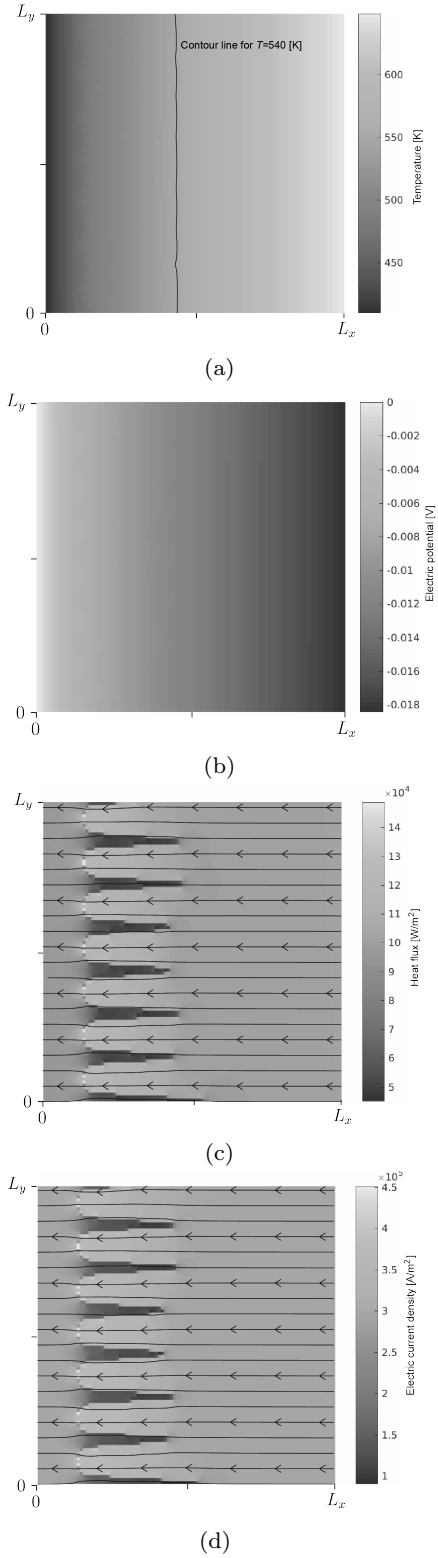

(a) (b) (c) (d)

Fig. 5: The temperature field [K] (a), the electric potential field [V] (b), the heat flux field [W/m^2] (c) and the electric current density field [A/m^2] (d) for the design solution solved for f_P and $h^{HC} = 821$ in Fig. 3c.

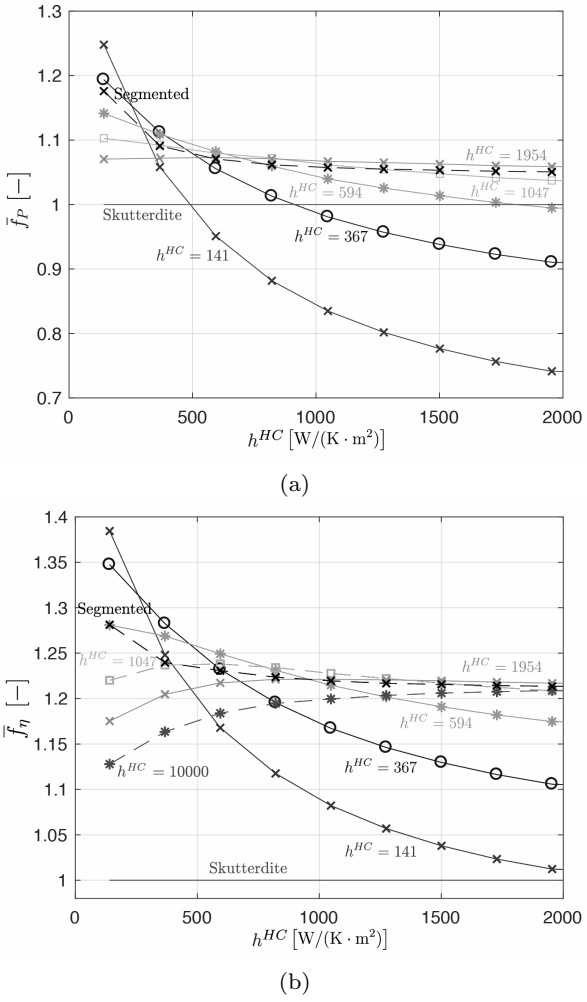

(a) (b)

Fig. 6: The design solutions solved for f_P (a) and f_η (b) (see Figs. 3 and 4, respectively) evaluated for different h^{HC}.

solutions are dependent on L_x. Furthermore, the design feature tendencies with respect to the amount of the two material phases in the f_P and f_η-design solutions are similar to the design features tendencies discussed in Sec. 3.2.

The relationships between the normalized electric power output, $\bar{f}_P = f_P / \max\left(f_P|_{h^{HC}=10000}\right)$, and device length, L_x, for the design solutions in Fig. 7 have been plotted in Fig. 9. For readability purposes, we have normalized the objectives with respect to the largest measured value of f_P for $h^{HC} = 10000$. The design solutions are optimized with the temperature constraint as in Sec. 3.1-3.2. The relationships between $\bar{f}_P$ and L_x are obtained by sweeping L_x in 100 equally sized steps in the interval $L_x \in [1; 10]$ [mm]. The largest $\bar{f}_P$ at the optimal thermoelectric module length, L_x^{opt}, for each h^{HC} has been marked with black dots in the plot. The design solutions

(a) (b) (c) (d) (e) (f)

Fig. 7: Designs solutions solved for f_P and length of the design domain, L_x [mm], equal to $L_x = 1$ (a), $L_x = 10$ (b), $L_x = 20$ (c), $L_x = 30$ (d), $L_x = 40$ (e) and $L_x = 50$ (f).

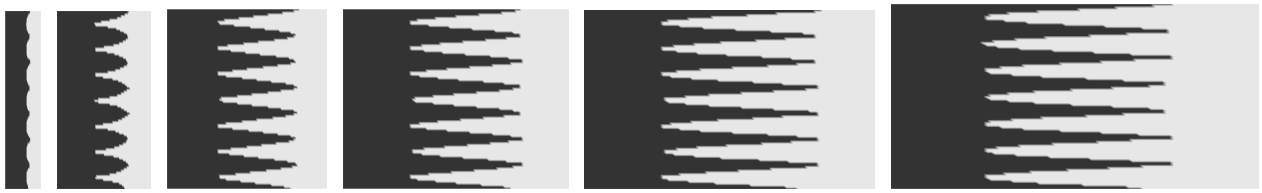

(a) (b) (c) (d) (e) (f)

Fig. 8: Designs solutions solved for f_η and length of the design domain, L_x [mm], equal to $L_x = 1$ (a), $L_x = 10$ (b), $L_x = 20$ (c), $L_x = 30$ (d), $L_x = 40$ (e) and $L_x = 50$ (f).

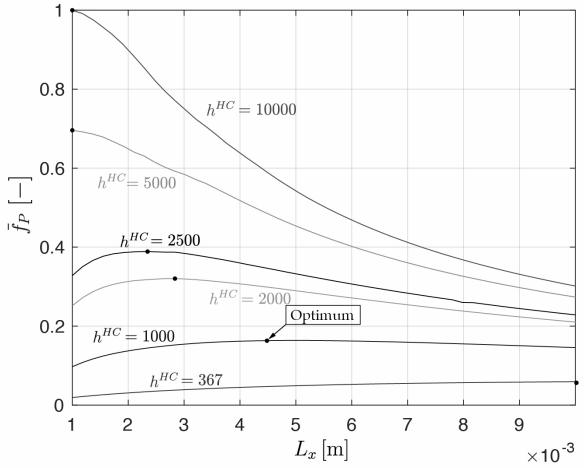

Fig. 9: The relationship between the normalized electric power output, $\bar{f}_P = f_P / \max\left(f_P|_{h^{HC}=10000}\right)$ and device length, L_x, for various values of h^{HC}. The black dots indicate the largest electric power output for a specific h^{HC}.

for different L_x illustrate several important relationships for the topology-optimized design solutions for TEGs: If $h^{HC} \to \infty$ and $L \to 0$ then $f_P \to \infty$. Furthermore, if $h^{HC} < \infty$ then there exists an optimum between f_P and L_x.

The relationship between f_P and L_x is an interaction between the Seebeck effect, the Joule heating effect and the finite thermal reservoirs at Γ^H and Γ^C. For finite magnitudes of h^{HC} and $L_x < L_x^{opt}$, the available thermal energy at Γ^{HC} is not effectively converted to electric energy, as the temperature difference between Γ^H and Γ^C, ΔT is decreased as $L_x \to 0$. As the temperature difference is decreased, the work done by the Seebeck effect is decreased entailing that $f_P \to 0$. For $h^{HC} = \infty$, which is equivalent to fixed temperature boundary conditions, we notice that $f_P \to \infty$ for $L_x \to \infty$. As $L_x \to \infty$ the temperatures at Γ^H and Γ^C approach T^H and T^C, however the Joule heating is also increased due to the larger internal electric resistance in the module. The compromise between the increasing work of the Seebeck effect and the Joule heating for $L_x \to \infty$ constitutes the interaction between L_x and f_P and causes the optima for f_P and L_x for finite h^{HC}.

With reference to the design solutions in Figs. 7 and 8, we notice that L_x stretch out two extremes with respect to the shapes of the spike-shaped design features: Design solutions solved for low L_x consist of sharp design features, whereas the design solutions solved for large L_x consist of rounded design features. The transitions between the material phases can be quantified by the function $\nu(x)$, which relates the y-directional averaged volume ratio of the materials along the spatial direction, x. The sharp design features, see e.g. Fig. 8c, constitute an almost linear relationship of $\nu(x)$ in the transition, whereas the rounded design features, see e.g. Fig. 7f, constitute a non-linear relationship of $\nu(x)$ in the transition.

The shapes, the extent and the position of the spike-shape design features are dependent on the temperatures of the reservoirs, the length of the design domains, the

magnitude of the temperature constraint, the convection coefficients and the material parameters. It may be possible to derive analytic expressions which relate all these parameters to the performance of the thermoelectric generators, however such study goes beyond the scope of this paper.

To conclude the section, we emphasize with reference to Figs. 7, 8 and 9 and the discussion above that L_x, the objective function and h^{HC} should be taken into account when designing TEGs.

3.6 Asymmetric hot and cold sides

As the final numerical example, we consider what we in this study denote *asymmetric boundary conditions*. Asymmetric boundary conditions are inspired by TEG applications where the flow type and flow conditions on Γ^H and Γ^C are different. Such applications are e.g. seen in applications where Γ^H is subjected to forced convection by water and Γ^C is subjected to natural convection by air or vice versa (confer with Tab. 2).

The importance of the design problem parameters is demonstrated in the design solutions in Figs. 10-11. The f_P-design solutions optimized for $h^C = 367$ and various h^H have been plotted in Fig. 10, and the f_P-designs solutions optimized for $h^H = 367$ and various h^C have been plotted in Fig. 11.

We notice that the design feature tendencies of the design solutions are similar to the design feature tendencies discussed in Sec. 3.2. However, when comparing Figs. 10-11, we emphasize one new and important design feature tendency: The design solutions for these asymmetric boundary conditions are indeed very different, for which reason it is critical to take the asymmetric heat transfer mechanisms into consideration when designing TEGs.

With reference to Figs. 10-11, we notice that the Skutterudite material phase is either pushed towards Γ^H or Γ^C when h^C and h^H are changed. This interplay occurs due to the interaction between the temperature constraint and the heat transfer rates. The heat transfer rates are related to the convection coefficients, and the convection coefficients govern the temperature distribution in Ω_D. Depending on the temperature distributions, the material phases are either pushed toward Γ^H or Γ^C to fulfill the temperature constraint and to maximize the performance of the device.

Similar to the design solutions solved for symmetric boundary conditions in Sec. 3.1 and 3.2, the spike-shaped design features are decreased as the convection coefficients are increased. The smaller absolute temperature difference between Γ^H and Γ^C in asymmetric design problems may explain that the transitions occur for larger convection coefficients for asymmetric design problems than symmetric design problems.

Nevertheless, the main message of this study is that asymmetric boundary conditions considerably change the design solutions, for which reason it is critical to take such model parameters into consideration when designing thermoelectric generators.

(a) (b) (c) (d) (e)

Fig. 10: Designs solutions solved for f_P, $h^C = 367$ and $h^H = 141$ (a), $h^H = 367$ (b), $h^H = 594$ (c), $h^H = 821$ (d) and $h^H = 1047$ (e)

(a) (b) (c) (d) (e)

Fig. 11: Designs solutions solved for f_η, $h^H = 367$ and $h^C = 141$ (a), $h^C = 367$ (b), $h^C = 594$ (c), $h^C = 821$ (d) and $h^C = 1047$ (e)

4 Discussion

In Figs. 3, 4, 7, 8, 10 and 11, we have demonstrated that density-based topology optimization can be utilized to improve the performance of segmented TEGs by introducing two dimensional design features. We have presented an application of a density-based topology optimization framework, which takes real material parameters, device dimensions and realistic boundary conditions into account. The study has demonstrated that topology optimization may be used to increase the performance of TEGs.

Due to the two-dimensional and spike-shaped design features, the topology optimized design solutions require significantly more effort to manufacture compared to the design solutions of the classical segmentation approach. However, the additional manufacturing effort and the fact that the predicted performance improvements only yield a maximum of 5-6% for the parameters investigated in this study, may indicate that the topology optimization approach may have minor practical application for this specific problem and material parameters.

Topology optimization may provide larger design improvements for other materials and/or thermoelectric coolers. We are currently working on a study which aims to report on this topic.

The contact resistance in the interface between the material phases is neglected in the finite element modelling. The thermal and electrical contact resistance has been shown to decrease the performance of both conventional and segmented thermoelectric modules in Bjørk [4]. Some topology optimized design solutions presented in this paper have a much greater contact area between the material phases than classically segmented design solutions, for which reason the predicted improvements may actually be smaller.

We include the following suggestions to future work: (1) A three dimension implementation of the methodology may provide larger design improvements as the design solutions may take advantage of three dimensional design features. (2) Multiple material phases may provide more advanced design features and performance improvements. (3) Other combinations of materials may provide larger performance improvements of the design solutions. (4) Deriving analytic expressions which relate the length of the spike-shaped design features, the choice of materials, the convection coefficients and the length of the designs may provide new and more insight in the pursuit of improving the performance of thermoelectric generators.

5 Conclusion

A density-based topology optimization approach for TEGs has been utilized to design the spatial layout of two real thermoelectric material phases, BiSbTe and

skutterudite, in order to optimize the electric power output and the conversion efficiency of thermoelectric generators. The study demonstrates that the spatial layout of the material phases depends on a large number of model parameters such as the length of the design domain and the convection coefficients at the surfaces at the hot and cold reservoirs. The topology optimized design solutions provide maximum performance improvements compared to classical segmented design solutions of 5-6% for low convection coefficients. The performance improvements are decreasing as the convection coefficients are increased, and for convection coefficients larger than a specific limit the topology optimized design solutions and the classical segmented design solutions have similar performance. Design problems solved for different convection coefficients on the surfaces of the hot and the cold reservoirs are significantly different, for which reason such effects should be taken into consideration when designing thermoelectric generators.

A temperature constraint on the BiSbTE material phase ensures that the temperature in this phase does not exceed 540 K. BiSbTE degenerates for temperatures above this limit. Details on the implementation are provided in App. 6 and can be added to the formulations in [8].

Two-dimensional, spike shaped design features are occurring for low convection coefficients. These design features are gradually diverging towards vertical one-dimensional transitions, seen in classical segmentation approaches, as the convection coefficients are increased.

The spike-shaped design features may enable parts of the design solutions to operate locally in an intermediate state between the two different material phases. This design feature indicates a realization of functionally graded materials.

An optimum between the electric power output and length of the design domain occurs for finite magnitudes of the convection coefficients. The optimal length of the design domain is determined by the spatial position of the material phases, the convection coefficients, and a compromise between the magnitude of Joule heating and the effectiveness of the Seebeck effect.

6 Appendix

In this section we provide details on the temperature constraint which is utilized to ensure that the temperature in the BiSbTe material phases of the design solutions do not exceed a specific magnitude, T_{max}. The constraint is an addition to the methodology presented in Lundgaard and Sigmund [8] and is given by:

$$f_C \leq \max(\mathbf{T}) \leq T_{max} \quad \forall \mathbf{T} \in \Omega_{\text{BiSbTe}} \tag{11}$$

where Ω_{BiSbTe} is the parts of the design solutions which consist of BiSbTe. The maximum temperature in the BiSbTe material phases, $\max(\mathbf{T}) \forall \mathbf{T} \in \Omega_{\text{BiSbTe}}$, can be approximated by the following expression in what we call the *finite element form*:

$$T_{max} \approx \left(\sum_{i \in \mathbb{O}_C} (T_i^e g_i(\rho_i))^p \right)^{\frac{1}{p}} \tag{12}$$

where $\mathbb{O}_C$ is the set of elements to be constrained, p is the temperature norm parameter and T_i^e is the temperature in the center of element i. To consider T_i^e instead of the nodal temperatures is convenient implementation-wise and the connection between the objective function and the temperature constraint is laid out straightforwardly. For very large temperature gradients, the element-wise evaluation of the temperatures may impose an unacceptable large error in the T_{max} approximation. However, for the boundary conditions and finite element discretizations considered in this study, the approximation is acceptable. $\mathbb{O}_C$ could in principle be a subset of Ω_D, however for the problems presented in this study, all elements in Ω_D in included in $\mathbb{O}_C$. The function $g(\rho_i)$ in Eq. (12) is given by:

$$g(\rho_i) = \frac{(-1+\rho_i)(1+q) g_{max} - g_{min}\rho_i}{q\rho_i - q - 1} \tag{13}$$

where g_{min} and g_{max} are the upper and lower bounds of $g(\rho_i)$ for $\rho_i \in [0;1]$, respectively, and q is the penalization parameter. The magnitudes of p and q are a compromise between numerically stability, well-posedness of the design problem, penalization of intermediate design variables and the precision of the T_{max} approximation in Eq. (12). The design solutions presented throughout this work are obtained for $p = 12$ [-], $q = 100$ [-], $T_{max} = 540$ [K], $g_{min} = 10^{-9}$ [-] and $g_{max} = 1$ [-]. The magnitude of g_{min} is a small number instead of zero to ensure numerical stability of the algorithm. The function g in Eq. (13) interpolates between g_{min} and g_{max} for $\rho \in [0;1]$: $g = 0$ if $\rho = 1$ and $g = 1$ if $\rho = 0$. Elements which are approaching the BiSbTe material phase, i.e. $\rho \to 0$, are subject to a larger weight in the p-norm approximation in Eq. (12) as $g \to 1$. If an element is not fulfilling the temperature constraint, the design variable of the specific element is pushed toward the skutterudite material phase in the following design iteration. To penalize intermediate design variables, q is chosen rather large, entailing that intermediate design variables are subject to a relatively large g which ensures that the designs solutions are pushed towards the extremes of the limits of ρ. The magnitude of q has been chosen with basis in numerical experiments.

The temperature constraint formulation in Eqs. (12)-(13) is inspired by the stress constraint work in [40], and Eq. (12)-(13) can in implementation form be written as:

$$f_C = \left(L_{\mathbb{Q}} \left(\mathbf{T}^e \circ \mathbf{g}\right)^p\right)^{\frac{1}{p}} \tag{14}$$

where $\circ$ denotes the Hadamard product (element wise multiplication), and $L_{\mathbb{Q}}$ is a vector consisting of zeros except for the positions $i \in \mathbb{O}_E$ which have the value unity. Eq. (14) is differentiated with respect to ρ and T. To simplify notation, we introduce the following terms for $\nabla_\rho f_C$:

$$\nabla_\rho f_C^1 = \mathbf{L}_{\mathbb{Q}}^T \circ \left(\left(\mathbf{T}^e \circ \mathbf{g}\right)^p\right)^{\frac{1}{p}} \tag{15}$$

$$\nabla_\rho f_C^2 = \frac{\left(\mathbf{T}^e \circ \mathbf{g}\right)^p \left(p \nabla_\rho \mathbf{g}\right)}{\mathbf{g}} \tag{16}$$

$$\nabla_\rho f_C^3 = p \mathbf{L}_{\mathbb{Q}} \circ \left(\mathbf{T}^e \circ \mathbf{g}\right)^p) \tag{17}$$

and $\nabla_T f_C$:

$$\nabla_T f_C^1 = \mathbf{L}_{\mathbb{Q}} \circ \left(\left(\mathbf{T}^e \circ \mathbf{g}\right)^p\right)^{\frac{1}{p}} \tag{18}$$

$$\nabla_T f_C^2 = \frac{\left(p\mathbf{T}^e \circ \mathbf{g}\right)^p \circ \nabla_T \mathbf{T}}{\mathbf{T}^e} \tag{19}$$

$$\nabla_T f_C^3 = p \mathbf{L}_{\mathbb{Q}} \circ \left(\mathbf{T}^e \circ \mathbf{g}\right)^p \tag{20}$$

$\nabla_\rho f_C$ and $\nabla_S f_C$ are now given by:

$$\nabla_\rho f_C = \frac{\nabla_\rho f_C^1 \circ \nabla_\rho f_C^2}{\nabla_\rho f_C^3} \tag{21}$$

$$\nabla_S f_C = \left\{ \begin{array}{c} \frac{\nabla_T f_C^1 \nabla_T f_C^2}{\nabla_T f_C^3} \\ \mathbf{0} \end{array} \right\} \tag{22}$$

which hereby provide all relevant terms in the adjoint sensitivity analysis. All division operators should be interpreted as element-wise divisions.

To demonstrate the influence of the temperature constraint in the design solutions, we have plotted a design solution with $T_{max} = 540$ [K] and $T_{max} = \infty$ for $h^{HC} = 1502$ [W/K·m^2] in Fig. 12. It is seen that the BiSbTE material phase for the temperature constrained design is pushed towards Γ^C to fulfill the constraint. The maximum temperature in the BiSbTE material phases for the $T_{max} = \infty$ and $T_{max} = 540$ design problems are 577.74 [K] and 540.02 [K], respectively. However, it is important to mention that the design solution in Fig. 12b is nonphysical because the material parameters of the BiSbTe material phase are not defined for temperatures above 540 K (confer with Fig. 2).

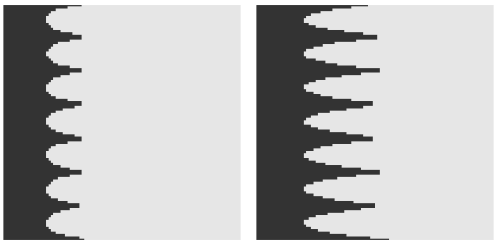

(a) $T_{max} = 540$ (b) $T_{max} = \infty$

Fig. 12: f_η-designs solutions solved for $h^{HC} = 1502$ with and without an active temperature constraint

References

1. David Michael Rowe. 1st edition, (CRC press, 2005).
2. Cronin B. Vining. *NAT MATER*, (2009). doi: https://doi.org/10.1038/nmat2361.
3. G. Jeffrey Snyder and Tristan S. Ursell. *PHYS REV LETT*, (2003). doi: 10.1103/PhysRevLett.91.148301.
4. Rasmus Bjørk. *J ELECTRON MATER*, (2015). doi: http://sci-hub.tw/10.1007/s11664-015-3731-7.
5. Martin Philip Bendsøe and Noboru Kikuchi. *COMPUT METHOD APPL M*, (1988). doi: https://doi.org/10.1016/0045-7825(88)90086-2.
6. Martin Bendsøe and Ole Sigmund. (Springer, 2003), 2nd edition.
7. E. E. Antonova and D. C. Looman. *INT CONF THERMOELECT*, (2005). doi: 10.1109/ICT.2005.1519922.
8. Chrisitan Lundgaard and Ole Sigmund. *STRUCT MULTIDISCIP O*, (2018). doi: 10.1007/s00158-018-1919-1.
9. Zhixi Bian and Ali Shakouri. *INT CONF THERMOELECT*, (2006). doi: 10.1109/ICT.2006.331365.
10. York Christian Gerstenmaier and Gerhard Wachutka. *J APPL PHYS*, (2017). doi: https://doi.org/10.1063/1.4994642.
11. Zhiting Tian, Sangyeop Lee, and Gang Chen. *ANN REV HEAT TRANSFER*, (2014). doi: 10.1615/AnnualRevHeatTransfer.2014006932.
12. Chrisitan Lundgaard and Ole Sigmund. *APPL ENERG*, *Accepted for publication*, (2018).
13. A Rezania, Kazuaki Yazawa, LA Rosendahl, and Ali Shakouri. *INT J THERM SCI*, (2013). doi: 10.1016/j.ijthermalsci.2013.05.002.
14. N. Wojtas and C. Hierold. (2013). doi: 10.1109/Transducers.2013.6627032.
15. Matthew M Barry, Kenechi A Agbim, and Minking K Chyu. *J ELECTRON MATER*, 44(6): 1394–1401, (2015). doi: http://sci-hub.tw/10.1007/s11664-014-3380-2.

16. Simon Bélanger and Louis Gosselin. *INT J ENERG RES*, (2011). doi: https://doi.org/10.1002/er.1820.
17. A Martínez, JG Vian, D Astrain, A Rodríguez, and I Berrio. *J ELECTRON MATER*, (2010). doi: http://sci-hub.tw/10.1007/s11664-010-1291-4.
18. Z Zhang, LN Chen, ZJ Chen, GQ Xiao, and ZJ Liu. *J ELECTRON MATER*, (2015). doi: http://sci-hub.tw/10.1007/s11664-015-3754-0.
19. Camille Favarel, Jean-Pierre Bédécarrats, Tarik Kousksou, and Daniel Champier. *ENERG CONVERS MANAGE*, (2016). doi: 10.13044/j.sdewes.2015.03.0020.
20. Xiaolong Gou, Heng Xiao, and Suwen Yang. *APPL ENERG*, (2010). doi: https://doi.org/10.1016/j.apenergy.2010.02.013.
21. J Esarte, G Min, and DM Rowe. *J POWER SOURCES*, (2001). doi: https://doi.org/10.1016/S0378-7753(00)00566-8.
22. Ryosuke O Suzuki, Yuto Sasaki, Takeyuki Fujisaka, and Min Chen. *J ELECTRON MATER*, (2012). doi: 10.1007/s11664-012-2074-x.
23. Jianlin Yu and Hua Zhao. *J POWER SOURCES*, (2007). doi: https://doi.org/10.1016/j.jpowsour.2007.07.045.
24. Rasmus Bjørk, Ali Sarhadi, Nini Pryds, N Lindeburg, and P Viereck. *ENERG CONVERS MANAGE*, (2016). doi: https://doi.org/10.1016/j.enconman.2016.04.042.
25. Ali Sarhadi, Rasmus Bjørk, Niels Lindeburg, Peter Viereck, and Nini Pryds. *ENERG CONVERS MANAGE*, (2016). doi: https://doi.org/10.1016/j.enconman.2016.04.052.
26. Yi Ma, Qing Hao, Bed Poudel, Yucheng Lan, Bo Yu, Dezhi Wang, Gang Chen, and Zhifeng Ren. *NANO LETT*, (2008). doi: 10.1021/nl8009928.
27. Andrew Muto, Jian Yang, Bed Poudel, Zhifeng Ren, and Gang Chen. *ADV ENERGY MATER*, (2013). doi: https://doi.org/10.1002/aenm.201200503.
28. TS Ursell and GN Snyder. *INT CONF THERMOELECT*, (2002). doi: 10.1109/ICT.2002.1190349.
29. Pham Hoang Ngan, Dennis Valbjørn Christensen, Gerald Jeffrey Snyder, Le Thanh Hung, Søren Linderoth, Ngo Van Nong, and Nini Pryds. *PHYS STATUS SOLIDI A*, (2014). doi: https://doi.org/10.1002/pssa.201330155.
30. SP Yushanov, LT Gritter, JS Crompton, and KC Koppenhoefer. Proceedings of the 2011 COMSOL Conference, Boston, USA, 2011.
31. Robert D. Cook, David S. Malkus, Michael E. Plesha, and Robert J. Witt. (John Wiley & Sons, 2007), 4th edition.
32. Panagiotis Michaleris, Daniel A Tortorelli, and Creto A Vidal. *INT J NUMER METH ENG*, (1994). doi: 10.1002/nme.1620371408.
33. James K Guest and Jean H Prévost. *INT J NUMER METH ENG*, (2006). doi: https://doi.org/10.1002/nme.1560.
34. Ole Sigmund. *STRUCT MULTIDISCIP O*, (2007). doi: http://sci-hub.tw/10.1007/s00158-006-0087-x.
35. Akihiro Sakai, Tsutomu Kanno, Kouhei Takahashi, Hiromasa Tamaki, Hideo Kusada, Yuka Yamada, and Hiroya Abe. *SCI REP-UK*, (2014). doi: http://dx.doi.org/10.1038/srep06089.
36. Wolfgang Seifert and Volker Pluschke. *PHYS STATUS SOLIDI A*, (2014). doi: 10.1002/pssa.201330392.
37. Y Yang, S H Xie, F Y Ma, and C H Lei. *J APPL PHYS*, (2012). doi: https://doi.org/10.1063/1.3674279.
38. W. Seifert, E. Müller, and S. Walczak. *INT CONF THERMOELECT*, (2006). doi: 10.1109/ICT.2006.331241.
39. York Christian Gerstenmaier and Gerhard Wachutka. *PHYS REV E*, (2012). doi: 10.1103/PhysRevE.86.056703.
40. Daniel M. De Leon, Joe Alexandersen, Jun S. Jun, and Ole Sigmund. *STRUCT MULTIDISCIP O*, (2015). doi: 10.1007/s00158-015-1279-z.